LJMU Research Online

Old, LJ, Balogh, ML, van der Burg, RFJ, Biviano, A, Yee, HKC, Pintos-Castro, I, Webb, K, Muzzin, A, Rudnick, G, Vulcani, B, Poggianti, B, Cooper, M, Zaritsky, D, Cerulo, P, Wilson, G, Chan, JCC, Lidman, C, McGee, S, Demarco, R, Forrest, B, De Lucia, G, Gilbank, D, Kukstas, E, McCarthy, IG, Jablonka, P, Nantais, J, Noble, A, Reeves, AMM and Shipley, H

 The GOGREEN survey: the environmental dependence of the star-forming galaxy main sequence at 1.0 < z < 1.5 (vol 493, 10.1093/mnras/staa579, 2020)

http://researchonline.ljmu.ac.uk/id/eprint/16434/

Article

For more information please contact researchonline@ljmu.ac.uk

The GOGREEN survey: the environmental dependence of the star-forming galaxy main sequence at 1.0 < z < 1.5

Lyndsay J. Old [1,2]★ Michael. L. Balogh,[3,4] Remco F. J. van der Burg,[5]
Andrea Biviano,[6,7] Howard K. C. Yee,[2] Irene Pintos-Castro,[2] Kristi Webb,[3,4]
Adam Muzzin,[8] Gregory Rudnick,[9] Benedetta Vulcani [10] Bianca Poggianti,[10]
Michael Cooper [11] Dennis Zaritsky [12] Pierluigi Cerulo,[13] Gillian Wilson,[14] Jeffrey
C. C. Chan [14] Chris Lidman [15] Sean McGee,[16] Ricardo Demarco,[13] Ben Forrest,[14]
Gabriella De Lucia [6] David Gilbank [17,18] Egidijus Kukstas [19] Ian G. McCarthy [19]
Pascale Jablonka,[20] Julie Nantais [21] Allison Noble,[22,23] Andrew M. M. Reeves[3,4]
and Heath Shipley[24]

Affiliations are listed at the end of the paper

ABSTRACT

We present results on the environmental dependence of the star-forming galaxy main sequence in 11 galaxy cluster fields at $1.0 < z < 1.5$ from the Gemini Observations of Galaxies in Rich Early Environments Survey (GOGREEN) survey. We use a homogeneously selected sample of field and cluster galaxies whose membership is derived from dynamical analysis. Using [O II]-derived star formation rates (SFRs), we find that cluster galaxies have suppressed SFRs at fixed stellar mass in comparison to their field counterparts by a factor of 1.4 ± 0.1 ($\sim 3.3\sigma$) across the stellar mass range: $9.0 < \log(M_*/M_\odot) < 11.2$. We also find that this modest suppression in the cluster galaxy star-forming main sequence is mass and redshift dependent: the difference between cluster and field increases towards lower stellar masses and lower redshift. When comparing the distribution of cluster and field galaxy SFRs to the star-forming main sequence, we find an overall shift towards lower SFRs in the cluster population, and note the absence of a tail of high SFR galaxies as seen in the field. Given this observed suppression in the cluster galaxy star-forming main sequence, we explore the implications for several scenarios such as formation time differences between cluster and field galaxies, and environmentally induced star formation quenching and associated time-scales.

Key words: galaxies: clusters: general – galaxies: evolution.

1 INTRODUCTION

Measurements of the galaxy stellar mass function and cosmic star formation rate (SFR) as a function of redshift have demonstrated that the global star formation activity of galaxies peaked at $z \sim 2$, declining until the present day (e.g. Madau & Dickinson 2014 and references therein). This evolution is also seen as a decrease in the specific SFR (sSFR) of galaxies with time since $z \sim 2$ (e.g. Whitaker et al. 2012 and others), and is characterized as evolution in the correlation between SFR and stellar mass, referred to as the star-forming main sequence (MS; Noeske et al. 2007). However,

comparing the evolution of the stellar mass functions for star-forming and quiescent galaxies separately (Peng et al. 2010; Muzzin et al. 2013) shows that a stellar mass-dependent 'quenching' of star formation must also be taking place. This quenching refers to a comparatively rapid terminal cessation of star formation that leads to the gradual build-up of the passively evolving galaxy population.

There is also evidence that the evolution of galaxies depends on their environment – whether this means local density, or their location as a satellite galaxy within a more massive host dark matter halo. At $z < 1$, galaxies in denser environments such as galaxy groups and galaxy clusters universally have lower fractions of star-forming galaxies than the field (e.g. Kauffmann et al. 2004; Balogh et al. 2004a; Cooper et al. 2006, 2007; Poggianti et al. 2006; Kimm

et al. 2009; Peng et al. 2010; von der Linden et al. 2010; Muzzin et al. 2012; Mok et al. 2013; Davies et al. 2016; Guglielmo et al. 2019; Pintos-Castro et al. 2019).

One explanation for this trend is that galaxies in groups and clusters are subject to additional processes that enhance the quenching rate (e.g. Balogh et al. 2004a; Peng et al. 2010; Wetzel et al. 2013). If this is the case, there should exist a transition galaxy population in groups and clusters that have low but non-zero SFRs. The bimodality in the galaxy colour and SFR distribution (e.g. Strateva et al. 2001; Baldry et al. 2004; Balogh et al. 2004b; Cassata et al. 2008; Wetzel, Tinker & Conroy 2012; Taylor et al. 2015) suggests that these transition galaxies are rare, implying a rapid transformation from the star forming to quiescent population. Identifying these transition galaxies from their lower than average SFRs requires large, carefully selected samples over a wide stellar mass range, and results todate are mixed. Several studies have claimed little to no trend in the star-forming MS with environment (e.g. Peng et al. 2010; Muzzin et al. 2012; Wetzel et al. 2012; Wijesinghe et al. 2012; Koyama et al. 2013); others find a modest trend in the sense that star-forming galaxies in denser environments have lower SFRs at fixed stellar mass than that of their counterparts in the field (e.g. von der Linden et al. 2010; Vulcani et al. 2010; Patel et al. 2011; Popesso et al. 2011; Haines et al. 2013; Paccagnella et al. 2016; Rodríguez del Pino et al. 2017; Wang et al. 2018).

In order to reconcile the modest, at best, differences between the SFRs of galaxies in groups, clusters and the field at low redshift with the fact that clusters host a much larger fraction of quenched galaxies, Wetzel et al. (2013) introduced a two-parameter model to describe the suppression of star formation for satellites in massive haloes. In this 'delayed-then-rapid' quenching scenario, as a satellite galaxy infalls into a cluster, there is a period of time within which a galaxy's SFR follows that of typical field galaxy evolution. After this 'delay-time', a galaxy experiences a swift truncation in its SFR.

Using a galaxy group/cluster catalogue (based on Yang et al. 2005) from the Sloan Digital Sky Survey Data Release 7 at $0.04 < z < 0.06$ (York et al. 2000; Abazajian et al. 2009), together with a high-resolution, cosmological N-body simulation to track satellite orbits, Wetzel et al. (2013) empirically fits a delayed-then-rapid quenching scenario where galaxy SFRs are unaffected for 2–4 Gyr following infall, after which star formation quenches rapidly. The long delay time is somewhat puzzling, given the shorter dynamical times associated with galaxy orbits. However, some authors (e.g. Muzzin et al. 2014; Taranu et al. 2014; Oman & Hudson 2016) find good agreement with models where quenching begins only when galaxies first pass within a small radius near the cluster core or where environmental quenching is driven by halting gas accretion (e.g. Fillingham et al. 2015).

A promising approach to better understand these results is to look at higher redshift clusters and groups. Because the dynamical time for a virialized system is shorter at higher redshift, and independent of halo mass (Tinker & Wetzel 2010; Tinker et al. 2013; McGee, Bower & Balogh 2014), we might hope to determine if these quenching time-scales are associated with orbital parameters. An alternative might be that they are determined by properties of the galaxy itself (e.g. gas content and SFR); these generally evolve at a different rate from the dynamical time, allowing us to break the degeneracy (McGee et al. 2014). Observations probing groups and clusters at intermediate redshifts are generally consistent with a total quenching time (i.e. the time between infall and cessation of star formation) that evolves approximately like the dynamical

time (e.g. Tinker & Wetzel 2010; Mok et al. 2014; Balogh et al. 2016; Foltz et al. 2018). However, there are indications that the *delay* time at $z \sim 1$ is shorter than would be expected from a simple scaling with dynamical time from $z \sim 0$ (McGee et al. 2014). These authors suggest that the high SFRs associated with galaxies coupled with mass-loaded winds at $z \sim 1$, means that they will exhaust their gas supply on a time-scale that is shorter than the dynamical time and hence quench before any orbit-related process like ram-pressure stripping can be effective. This phenomenon, called 'overconsumption', also proves to be a good match to the stellar mass dependence of the observed quenched galaxy fraction at $z \sim 1$ (Balogh et al. 2016; Fossati et al. 2017; Kawinwanichakij et al. 2017; Chartab et al. 2019).

It is therefore interesting to extend this work to even higher redshift, $z > 1$, where galaxies are significantly younger, have higher SFRs and lower depletion time-scales (e.g. Tacconi et al. 2013, 2018). While there are pioneering studies of galaxy clusters at higher redshifts (e.g. $z > 1$; Strazzullo et al. 2006; Gobat et al. 2008; Snyder et al. 2012; Lotz et al. 2013; Martini et al. 2013; Nantais et al. 2013; Zeimann et al. 2013; Newman et al. 2014; Stanford et al. 2014; Nanayakkara et al. 2016; Nantais et al. 2017; Strazzullo et al. 2019), deep spectroscopic cluster studies of galaxies of all types for a range of halo masses do not currently exist, and the typical properties of cluster galaxies at this epoch are still unknown.

The goal of this study is to measure the difference in the star-forming galaxy MS between cluster and field galaxies with a deep spectroscopic sample of homogeneously targeted galaxies above $z > 1$. For this purpose, we use the recently completed Gemini Observations of Galaxies in Rich Early ENvironments (GOGREEN) survey (Balogh et al. 2017). In Section 2, we describe the key survey details including the cluster sample and some aspects of the data reduction. In Section 3, we present results on the environmental dependence of the star-forming MS and the corresponding discussion in Section 4. We conclude our findings in Section 5. Throughout the paper, we adopt a flat Λ cold dark matter cosmology with $\Omega_m = 0.3$, and a Hubble constant of $H_0 = 70$ km s^{-1} Mpc^{-1}. We also assume a Chabrier initial mass function (IMF; Chabrier 2003).

2 THE GOGREEN SURVEY

The GOGREEN survey[1] is based on a Gemini Large and Long Program using the GMOS instruments (Murowinski et al. 1998; Hook et al. 2004) on Gemini North and South telescopes to obtain unbiased multiobject spectroscopy of galaxies of all types down to stellar masses $M_* \sim 10^{10.3} M_\odot$. The survey targets 21 systems spanning a wide range in halo mass at $1.0 < z < 1.5$. In addition to deep spectroscopy, the GOGREEN survey has obtained over 100 h of *UBVRIzYJK* and IRAC 3.6 μm imaging for the majority of the target fields, providing photometric products including stellar masses, accurate rest-frame *UVJ* colour measurements and characterization of spectroscopic completeness. Crucially, the survey is designed to produce a field sample of comparable size to that of the targeted groups and clusters, selected under the same conditions.

One of the key science goals of GOGREEN is to probe environmental quenching and the growth of the stellar mass function at this early epoch. The survey is also designed to examine the stellar populations and dynamics of galaxies in clusters that span

---

[1]A list of all GOGREEN papers can be found on the following webpage: http://gogreensurvey.ca/data-releases/publicationspress/.

Table 1. This table summarizes the key properties of the 11 clusters used in this study that are targeted by the GOGREEN survey. z_c is the initial cluster mean redshift estimate, taken from Balogh et al. (2017), with the exception of SpARCS0219, for which the z_c estimates have been obtained using the peak of the z distribution. N_{tot} is the number of objects with good-quality redshifts in the cluster field from either GOGREEN or the literature, avoiding double entries, and N_{mem} is the number of galaxies that are considered as members by at least one of the two C.L.U.M.P.S and Clean algorithms. σ_{los} is the rest-frame line-of-sight velocity dispersion of the cluster obtained by using the galaxy membership probabilities as weights. Finally, r_{200c} is the overdensity radius of the cluster (where the overdensity 200 times critical at the cluster redshift), estimated from σ_{los} using equation (B3) in Mamon, Biviano & Boué (2013).

Cluster name	RA $_{J2000}^{BCG}$	DEC $_{J2000}^{BCG}$	z_c	N_{tot}	N_{mem}	σ_{los} (km s^{-1})	r_{200c} (Mpc)
SPT–CLJ0205–5829	02:05:48.19	−58:28:49.0	1.320	70	28	678 ± 57	0.76 ± 0.09
SPT–CLJ0546–5345	05:46:33.67	−53:45:40.6	1.067	103	67	977 ± 68	1.17 ± 0.09
SPT–CLJ2106–5844	21:06:04.59	−58:44:27.9	1.132	81	50	1055 ± 83	1.23 ± 0.10
SpARCS0035–4312	00:35:49.68	−43:12:23.8	1.335	129	29	840 ± 52	0.93 ± 0.07
SpARCS0219–0531	02:19:43.56	−05:31:29.6	1.325	56	9	810 ± 77	0.79 ± 0.12
SpARCS0335–2929	03:35:03.56	−29:28:55.8	1.368	133	27	542 ± 33	0.67 ± 0.08
SpARCS1034 + 5818	10:34:49.47	+ 58:18:33.1	1.386	40	11	250 ± 28	0.24 ± 0.03
SpARCS1051 + 5818	10:51:11.23	+ 58:18:02.7	1.035	185	42	689 ± 36	0.88 ± 0.07
SpARCS1616 + 5545	16:16:41.32	+ 55:45:12.4	1.156	214	60	782 ± 39	0.92 ± 0.06
SpARCS1634 + 4021	16:34:37.00	+ 40:21:49.3	1.177	190	69	715 ± 37	0.85 ± 0.06
SpARCS1638 + 4038	16:38:51.64	+ 40:38:42.9	1.196	174	56	564 ± 30	0.70 ± 0.06

a wide range in halo mass at $1.0 < z < 1.5$ when the Universe was <6 Gyr old. Candidate groups and clusters are selected in three approximate bins of mass: groups ($M < 10^{14} M_\odot$), typical clusters ($10^{14} < M/M_\odot < 5 \times 10^{14}$), and very massive clusters ($M > 5 \times 10^{14} M_\odot$). Within GOGREEN, we target nine group mass candidates in the COSMOS (Finoguenov et al. 2007; George et al. 2011) and Subaru XMM Deep Survey (SXDS; Finoguenov et al. 2010) fields, nine typical clusters from the *Spitzer* Adaptation of the Red-sequence Cluster Survey (SpARCS; Muzzin et al. 2009; Wilson et al. 2009; Demarco et al. 2010), five of which have extensive GMOS spectroscopic follow-up from the Gemini Cluster Astrophysics Spectroscopic Survey (GCLASS; Muzzin et al. 2012), and we target three very massive clusters from the South Pole Telescope (SPT) survey (Brodwin et al. 2010; Foley et al. 2011; Stalder et al. 2013). In this study, we focus on eleven of the GOGREEN clusters, the properties of which are described in Section 2.3 and summarized in Table 1.

2.1 Spectroscopic data

In this section, we summarize the relevant spectroscopic observations, spectroscopic targeting, and reduction for the data used in this study. Full details are given in the survey description paper (Balogh et al. 2017) and a forthcoming data release paper (Balogh et al. in preparation). Spectroscopic targets were selected using magnitude and colour cuts from combined deep GMOS z'-band imaging and *Spitzer* IRAC 3.6 μm photometry. The GMOS z'-band imaging was obtained as part of the GOGREEN programme, and 5σ depths range from 24.75 to 25.70 for the 11 GOGREEN clusters used in this study. More details regarding the integration time, condition, and depths for each individual field can be found in Balogh et al. (2017).

We focus on 11 of the 12 GOGREEN cluster fields, omitting the twelfth GOGREEN cluster, SpARCS1033, from this analysis, as the K-band observations are not yet complete. We complemented our own deep 3.6 μm *Spitzer* IRAC imaging with publicly available imaging (5σ AB depth of at least 2 μJy or AB = 23.1) from SERVS (Mauduit et al. 2012), S-COSMOS (Sanders et al. 2007), and SpUDS (Galametz et al. 2013), and additional CO programmes (PI: Menanteau, PID = 70149; PI: Brodwin, PIDs = 60099, 70053).

Targeted galaxies are selected to have total magnitudes of [3.6] < 22.5 and $z' < 24.25$, avoiding low-redshift ($z < 1$) contamination by imposing a colour cut determined using the colour–magnitude distribution of galaxies with high-quality photometric redshifts in UltraVISTA (Muzzin et al. 2013). Spectroscopic slit masks were designed in order to obtain high numbers of bright and faint galaxies while also ensuring reasonable completeness in the cluster core. For further details regarding mask design and for technical details regarding data reduction, we refer the reader to section 2.4.3 and section 3 in Balogh et al. (2017).

Most observations were obtained with the upgraded Hamamatsu detectors on GMOS-N and GMOS-S (Gimeno et al. 2016), though some of the earliest data taken on Gemini-N used the older EEV deep depletion detectors. All fields were observed with the R150 grating to maximize the wavelength coverage (observed wavelength range of the spectra is ~ 5500–10 500 Å) on the detector and ensure high-redshift completeness. Nod-and-shuffle mode was used to ensure good sky subtraction at red wavelengths, and to maximize slit density in the cluster cores. All observations were obtained with the detector binned 2×2, delivering a dispersion of 3.8 Å pixel^{-1} for the Hamamamatsu detectors and 3.5 Å pixel^{-1} for the EEV detector. With slit widths of 1 arcsec, the resulting spectral resolving power is $R \sim 460$ (with spectral resolution ~20 Å pixel^{-1}). A relative flux calibration is applied to the spectra based on standard star observations taken once per semester. Absolute flux calibration is described in Section 2.2. Telluric absorption is corrected using MOLECFIT (Kausch et al. 2015; Smette et al. 2015), and redshifts are computed via cross-correlation with a variety of templates, using MARZ (Hinton et al. 2016).

GOGREEN deliberately builds upon the previous lower redshift galaxy cluster survey GCLASS (Muzzin et al. 2009; Wilson et al. 2009; Demarco et al. 2010), for which data were taken in a very similar manner (similar exposure times), and we incorporate GMOS spectroscopy for five of the $z > 1$ clusters from that survey in our analysis.

2.2 Photometric data

We use K-band selected photometric catalogues derived from deep, multiband imaging (van der Burg et al. in preparation).

Stellar masses are derived from SED fitting to multiwavelength photometry, using FAST (Kriek et al. 2009, 2018) and stellar population synthesis models from Bruzual & Charlot (2003). A Chabrier IMF (Chabrier 2003), solar metallicity, and the dust law from Calzetti et al. (2000) are assumed. The star formation history (SFH) is parametrized as SFR $\propto e^{-t/\tau}$, where τ ranges between 10 Myr and 10 Gyr, and the age is left as a free parameter. We note that stellar masses derived from non-parametric SFHs have been found to be typically ~0.2 dex higher than those derived in this work (Leja et al. 2019a, b; Webb et al. in preparation).

To obtain an absolute calibration for the GOGREEN spectra, we use the appropriate *I*-band photometry. We first interpolate the filter response curve, *R*, to match the spectral wavelength distribution using cubic-spline interpolation. We then integrate over the interpolated filter response curve multiplied by the spectral flux, f_λ, to give the total spectral flux:

$$f_{\text{tot}} = \int_{\lambda_{\text{min}}}^{\lambda_{\text{max}}} (R f_\lambda \lambda \, \mathrm{d}\lambda) / \int_{\lambda_{\text{min}}}^{\lambda_{\text{max}}} (R \lambda \, \mathrm{d}\lambda) . \tag{1}$$

After converting this spectral flux in wavelengths to frequency, we then multiply the entire spectra by the ratio of the spectral flux and the total *I*-band flux derived from the photometry to obtain flux-calibrated spectra corrected for slit losses.

2.3 Cluster membership

We use the dynamical properties of the galaxies to select those that are cluster members, employing two methodologies. One approach, referred to as the Clean algorithm (Mamon et al. 2013), uses an estimate of the cluster line-of-sight velocity dispersion, σ_{los}, to predict the cluster mass from a scaling relation. The other algorithm, referred to as C.L.U.M.P.S (Munari et al. in preparation) is based on the Shifting Gapper (SG) method of Fadda et al. (1996). In this paper, cluster members are defined as those that are identified by either the Clean or C.L.U.M.P.S algorithm. We refer the reader to Section A in the appendix for more details regarding these membership algorithms.

In Table 1, we list the cluster mean redshift $\bar{z}$, the number of objects with good-quality redshifts in the cluster field from either GOGREEN or the literature, N_{tot}, and the number of member galaxies that are considered members by at least one of the two C.L.U.M.P.S and Clean algorithms, N_{mem}. We also include the rest-frame line-of-sight velocity dispersion, σ_{los}, derived from this dynamical membership procedure, and an estimate of r_{200c} for each cluster in Table 1. We note that our spectroscopic targeting extends beyond r_{200c}, but does not equally sample the area beyond this radius. Throughout this paper, the centre of the cluster is taken as the location of the BCG when available. In this work, the BCG is defined as the most massive galaxy with photometric redshift consistent with the cluster mean redshift, and projected within 500 kpc from the main galaxy overdensity (for more details, we refer the reader to van der Burg et al. in preparation). We note that excluding potential active galactic nucleus (AGN) candidates (identified via several diagnostics) produces no qualitative change in our results. From works such as Martini et al. (2013), we expect a consistent AGN fraction in our cluster galaxy sample with respect to the field at $1.0 < z < 1.5$. We also note that the expected fraction in clusters is small (e.g. <0.1) and that many of these AGNs are likely to be in early-type galaxies (e.g. Kauffmann et al. 2003).
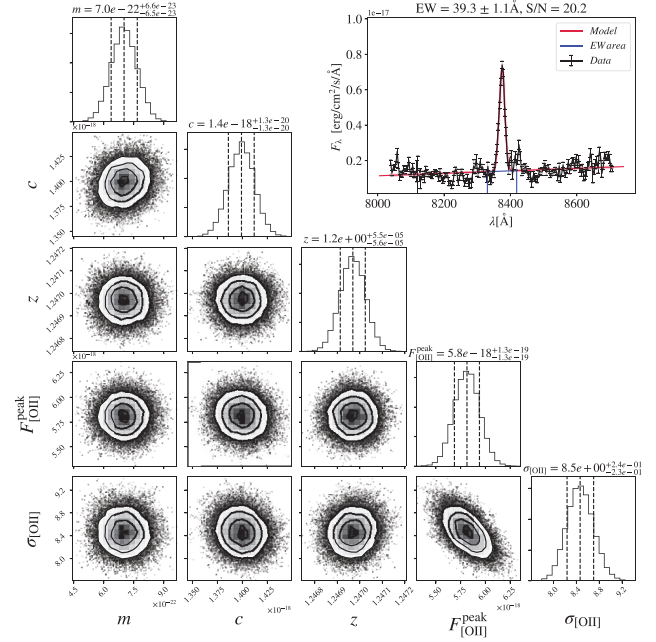
Figure 1. Example of the marginalized probability distributions produced by our MCMC analysis of [O II] emission for the five parameter model of a composite of a linear continuum and a Gaussian emission line. The parameters are the slope (*m*), the intercept (*c*), the galaxy redshift (*z*), the peak flux of the emission ($F_{[\text{O II}]}^{\text{peak}}$), and the width of the [O II] emission line ($\sigma_{[\text{O II}]}$).

2.4 O II detection

We take a Bayesian model selection approach in detecting [O II] emission in the GOGREEN galaxy spectra. Separately, we fit two models to the data, with the first assuming a linear continuum and the second assuming a composite of a linear continuum and a Gaussian emission line according to

$$f_{\text{model}}(\lambda) = m \, \lambda + c + \mathcal{N}\left(\lambda_{[\text{O II}]}(1+z) | F_{[\text{O II}]}^{\text{peak}}, \sigma_{[\text{O II}]}\right). \tag{2}$$

Both models depend on the following three parameters: *m* and *c* are the slope and intercept of the continuum, and *z* is the galaxy redshift. The second model also depends on two parameters describing the Gaussian-shaped emission: $F_{[\text{O II}]}^{\text{peak}}$ is the peak flux of the emission and $\sigma_{[\text{O II}]}$ is the width of the [O II] emission line. We assume that our uncertainties follow a normal distribution, and therefore our likelihood function for both models is

$$\ln \mathcal{L} = -\frac{1}{2} \sum_{i=1}^{n} \left(\frac{f_i - f_{\text{model}}}{\sigma_i}\right)^2 = -\frac{1}{2} \chi^2 . \tag{3}$$

We employ EMCEE, an affine-invariant ensemble sampler for Markov chain Monte Carlo (MCMC), to efficiently explore our parameter space and determine the posteriors of the model parameters (Foreman-Mackey et al.). We utilize 50 walkers and perform 800 iterations per model per spectrum (including a 'burn-in' of 300 iterations), assuming flat priors for model parameters. We fit a section of the spectra within the wavelength range of ±150 Å from the predicted location of the [O II] emission line given the galaxy redshift. An example of the marginalized probability distributions produced by our MCMC analysis for the five-parameter model is demonstrated in Fig. 1. We use Bayesian Information Criterion (BIC) as a criterion for model selection among the two models
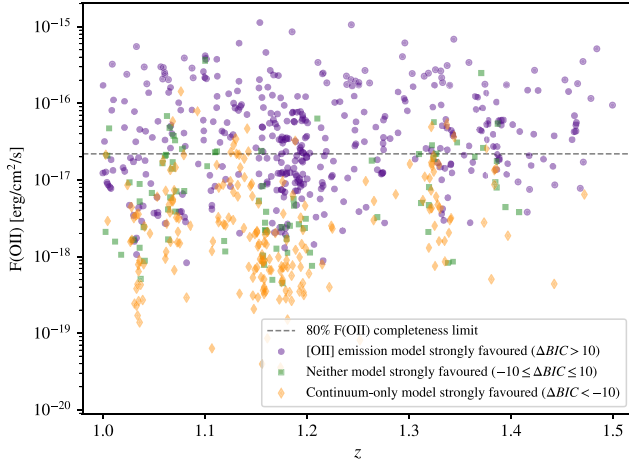
Figure 2. Galaxy redshift and $F([O\,\textsc{ii}])$ where points are colour coded by the ΔBIC criteria described in Section 2.4. Galaxies where the model including both a continuum and an [O\,\textsc{ii}] emission line are strongly favoured over a model with just a continuum are represented as purple circles. Galaxies where neither model is strongly favoured are represented as green squares, and galaxies where the continuum-only model is strongly favoured are represented as dark orange diamonds. The 80 per cent flux completeness limit, $F([O\,\textsc{ii}]) = 2.2 \times 10^{-17}\,\mathrm{erg\,cm^{-2}\,s^{-1}}$, is shown as a dashed grey line. Galaxies above this flux limit are selected as star forming and are used for the subsequent analysis.

described above, one which assumes an emission line is present at the expected rest-frame wavelength of [O\,\textsc{ii}], and one which assumes there is no emission line present at the rest-frame wavelength of [O\,\textsc{ii}]. BIC is based on the likelihood function, and takes into account the number of parameters in a model so as to penalize models with more parameters to avoid a possible increase in the likelihood solely by increasing the number of parameters (Schwarz 1978). The form for calculating the BIC is

$$\mathrm{BIC} = k\ln(n) - 2\ln(\hat{\mathcal{L}}) \,, \tag{4}$$

where n is the number of data points, k is the number of parameters estimated by the model, and $\hat{\mathcal{L}}$ is the maximum value of the likelihood function of the model. The model with the lowest BIC is preferred, with the degree of model favourability adopted by the classification of Kass & Raftery (1995), which takes into account the ΔBIC. We take a conservative approach, adopting a criterion of $\Delta BIC > 10$ to ensure that the model with an emission line is favoured only with 'very strong' evidence against higher BIC. Cases for which $\Delta BIC < 10$ indicate that evidence for supporting a model where an emission line is weak or evidence for a model without an emission line is preferred. In Fig. 2, we show the galaxy redshift and $F([O\,\textsc{ii}])$ for all galaxies (regardless of membership), where points are colour coded by the ΔBIC criteria. We note that adjusting these criteria from 'very strong' evidence to 'strong' evidence ($\Delta BIC > 6$) has little effect on the number distributions of objects in these categories.

To deduce the minimum [O\,\textsc{ii}]-derived flux, $F([O\,\textsc{ii}])$, with which to securely select [O\,\textsc{ii}] detections, we bin galaxies by flux and calculate the percentage of galaxies within each flux bin where the emission-line model is very strongly favoured according to the BIC criterion. We then fit this relation between flux and ratio of model criterion with a fourth-degree polynomial and define the minimum $F([O\,\textsc{ii}])$ as the flux at which this percentage reaches 80 per cent. With this conservative limit of $F([O\,\textsc{ii}]) = 2.2 \times$

$10^{-17}\,\mathrm{erg\,cm^{-2}\,s^{-1}}$, there are 262 total [O\,\textsc{ii}] detections, including 100 cluster galaxies and 162 field galaxies.

2.5 [O\,\textsc{ii}]-derived SFRs

The [O\,\textsc{ii}]-derived SFRs for the GOGREEN galaxies are calculated from the measured [O\,\textsc{ii}] luminosities according to the relation from Gilbank et al. (2010), where

$$\mathrm{SFR_0}/\left(\mathrm{M_\odot\,yr^{-1}}\right) = L([O\,\textsc{ii}])/(3.80 \times 10^{40}\,\mathrm{erg\,s^{-1}}) \,. \tag{5}$$

We use the empirical correction derived from Hα to correct this nominal SFR ($\mathrm{SFR_0}$) for the metallicity and dust dependence of [O\,\textsc{ii}] luminosity on SFR as a function of stellar mass, such that corrected SFR is given by

$$\mathrm{SFR} = \frac{\mathrm{SFR_0}}{a\,\tanh[(x-b)/c] + d} \,, \tag{6}$$

where $x = \log(M_*/\mathrm{M_\odot})$, $a = -1.424$, $b = 9.827$, $c = 0.572$, and $d = 1.700$. For more details regarding the empirically derived correction, we refer to Gilbank et al. (2010). The SFR calibration assumes a Kroupa IMF, while the stellar masses were measured with a Chabrier IMF, so we apply a conversion from a Kroupa IMF to a Chabrier IMF (Kroupa $= 1.122$ Chabrier) to ensure consistency with the galaxy stellar mass measurements (e.g. Cimatti et al. 2008). While the Gilbank et al. (2010) relation is derived for lower redshift objects, Sobral et al. (2012) and Hayashi et al. (2013) demonstrate that Hα and [O\,\textsc{ii}] luminosities correlate well at higher redshifts ($z \sim 1.5$), though indications are that galaxies are somewhat less dust extincted for a given Hα luminosity compared with low redshift. As long as the abundance and properties of dust are not environment dependent, this should not alter our conclusions about the relative SFR in cluster and field galaxies. However, if the average dust content of cluster galaxies is lower than that of field galaxies (as is hinted by McGee & Balogh 2010; Zeimann et al. 2013), we would expect lower intrinsic SFRs for cluster galaxies (see also Gallazzi et al. 2009). We discuss this further in Section 3. We have checked that SFRs derived from [O\,\textsc{ii}] correlate with SFRs derived from Hα for a very small subset of the [O\,\textsc{ii}] detections for which Hα measurements are available from *HST*/WFC3 G141 grism spectroscopy from Matharu et al. (2019). We also note that the [O\,\textsc{ii}]-derived GOGREEN star-forming MS and the distributions of SFR with respect to the star-forming MS are remarkably similar to those from an Hα-derived galaxy sample at a similar epoch (we refer the reader to Section 4.1 and Appendix B for further details).

In Fig. 3, we show that this sample of star-forming galaxies has predominantly blue colours in *UVJ* colour–colour space. We note that making an additional selection to exclude red galaxies from the sample does not qualitatively change our results.

2.6 Cluster and field sample properties

In Fig. 4, we present the stellar mass and redshift distributions of the cluster and field sample. In this [O\,\textsc{ii}]-emitting galaxy sample, field galaxies generally sit at lower stellar masses than the cluster galaxies. For this reason, we perform the subsequent analyses in bins of stellar mass. In Fig. 4, it is also clear that while the mean redshifts of the two samples are very similar ($\Delta <z> =0.01$), the shapes of the distributions are quite different. The cluster galaxies are situated in the redshift space of individual clusters, whereas the field
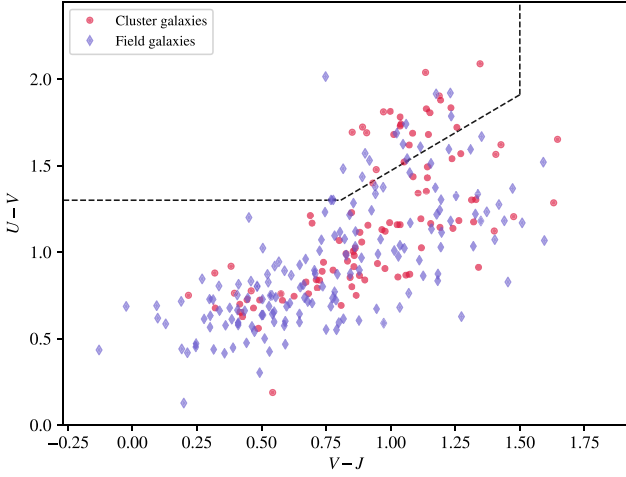
Figure 3. *UVJ* diagram of [O II] emitters with classifications from Muzzin et al. (2013) for $1 < z < 4$ (adapted from Williams et al. 2009), where quiescent galaxies are above the dashed line in the upper left region, and star-forming galaxies are below the dashed line.
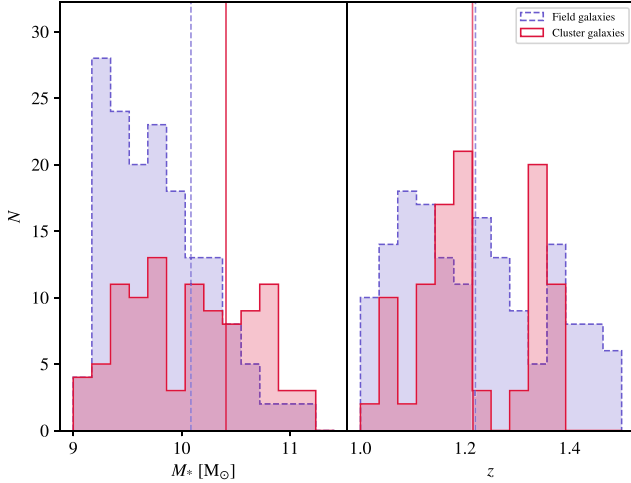

Figure 4. The stellar mass (*left*) and redshift (*right*) distributions for the field (dashed purple) and cluster (solid crimson) samples. The vertical lines represent the mean stellar mass and mean redshift of the cluster and field galaxy populations.

galaxies span a wider and more homogeneous redshift distribution.[2] To ensure any difference in the star-forming MS between cluster and field is not due to differences in the underlying redshift distribution between our cluster and field samples, we apply a correction to the mean field SFR according to the mean redshift difference in cluster and field in each stellar mass bin. The correction is calculated using the observed cosmic star formation redshift relation for field galaxies from Schreiber et al. (2015):

$$\log_{10}\left(\text{SFR}_{\text{MS}}\left[\text{M}_\odot\text{yr}^{-1}\right]\right) = m - m_0 + a_0 r - a_1$$
$$\times[\max(0, m - m_1 - a_2 r)]^2, \qquad (7)$$

[2]A two-sample KS test rejects that these two samples are drawn from the same stellar mass distribution with a *p*-value of 0.00017. The two-sample KS test *p*-value for the field and cluster redshift samples is found to be 0.06.
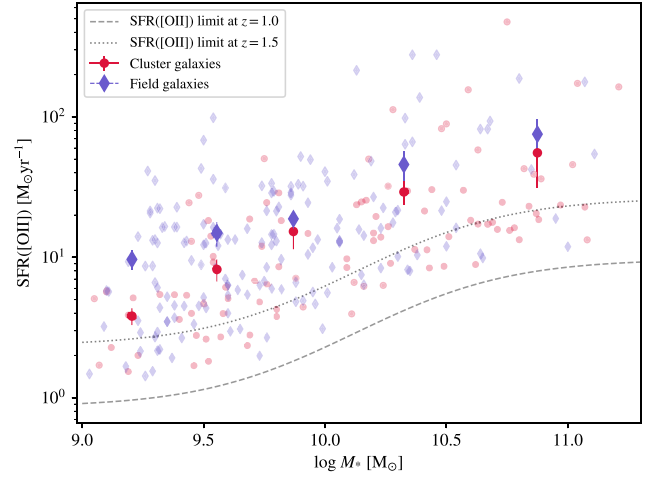
Figure 5. The MS of star formation of cluster galaxies versus field galaxies in the GOGREEN fields. The solid purple and crimson markers signify the mean field SFRs and the cluster galaxy SFRs in each stellar mass bin, respectively. The field SFRs have been corrected using the cosmic SFR versus z relation of equation (7) in order to match the mean redshift of cluster galaxies within each stellar mass bin. The error bars represent the bootstrap standard error from bootstrap resampling the data within each bin. The dashed and dotted grey lines represent the SFRs that correspond to the 80 per cent flux completeness limit at $z = 1.0$ and $z = 1.5$, respectively.

where $r \equiv \log_{10}(1 + z)$, $m \equiv \log_{10}(M_*/10^9 \ \text{M}_\odot)$, with $m_0 = 0.5 \pm 0.07$, $a_0 = 1.5 \pm 0.15$, $a_1 = 0.3 \pm 0.08$, $m_1 = 0.36 \pm 0.3$, and $a_2 = 2.5 \pm 0.6$. We note that the size of this correction is smaller than the statistical error bars in Fig. 5.

3 RESULTS

In Fig. 5, we present the star-forming galaxy MS for cluster galaxies in the GOGREEN sample (crimson circles) and galaxies in the field (purple diamonds). We show the mean SFR of cluster and field galaxies (solid, larger data points with error bars) in bins of stellar mass where bin widths are chosen adaptively to maintain a similar number of objects in each stellar mass bin. The error bars represent the bootstrap standard error.

From this comparison, we identify a modest environmental dependence on the star-forming galaxy MS: cluster galaxy SFRs are lower than their counterparts in the field at fixed stellar mass. To quantify this difference, we first fit the observed MS for the full sample using the Theil–Sen estimator (Theil 1950; Sen 1968) for robust linear regression of the relation between $\log(M_*)$ and $\log(\text{SFR})$. We then use this main-sequence relation to calculate a $\Delta\text{SFR}_{\text{MS}}$ distribution for both the cluster galaxy and the field galaxy samples.

The cluster and field $\Delta\text{SFR}_{\text{MS}}$ distributions are shown in Fig. 6, where the solid crimson vertical line represents the mean cluster galaxy $\Delta\text{SFR}_{\text{MS}}$ and the dashed purple vertical line represents the mean field galaxy $\Delta\text{SFR}_{\text{MS}}$. The mean difference in $\log(\Delta\text{SFR}_{\text{MS}})$ between the cluster and field[3] is $-0.145 \ \text{M}_\odot \ \text{yr}^{-1}$. Dividing by the combined bootstrap standard error (0.045 dex) yields a significance

[3]We exclude one cluster galaxy and three field galaxies whose $\Delta\text{SFR}_{\text{MS}}$ is more than 2σ outside this fit to avoid these extreme values of ΔSFR from dominating the comparison of different populations.
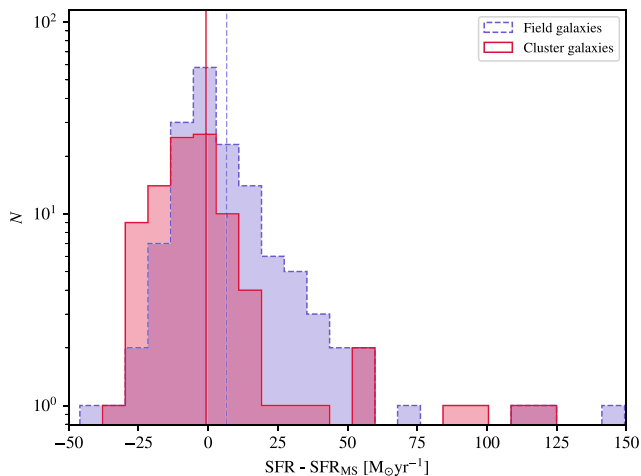
Figure 6. Cluster and field ΔSFR_{MS} distributions. The solid crimson vertical line represents the mean cluster galaxy ΔSFR_{MS}, and the dashed purple vertical line represents the mean field galaxy ΔSFR_{MS}.

of $\sim 3.3\sigma$.[4] A two-sample KS test rejects that these two samples come from the same distribution with a *p*-value of 1.4×10^{-5}. We see a similar difference in the specific SFRs of the samples, with a difference in average $\log(sSFR)$ of -0.128 ± 0.046 dex at the $\sim 2.8\sigma$ level. We now focus on the shape of the ΔSFR_{MS} distributions. We see that the cluster population has a small tail to lower SFRs. The most significant difference is the near absence of cluster galaxies with significantly enhanced SFRs, although these galaxies are common in the field.

We note that the small correction we make to account for the different mean redshifts of the two samples using the Schreiber et al. (2015) as described in Section 4 does not have a significant effect on these results. However, the fixed [O II] flux limit corresponds to a different SFR limit at $z = 1.0$ and $z = 1.5$. Because of the different redshift distributions of the cluster and field samples, this can lead to a difference that is not accounted for by this correction. To be even more conservative, if we select a subsample for which the SFR is greater than that corresponding to the 80 per cent flux completeness limit at $z = 1.5$, we reduce the sample to 64 cluster and 130 field galaxies, but find the same qualitative trend between cluster and field at the $\sim 2.4\sigma$ level.

Separating the sample by redshift, we find that our result is driven by the lower redshift end of the sample.[5] At $z < 1.3$, the significance of the difference between cluster and field $\log(\Delta SFR_{MS})$ and $\log(\Delta sSFR_{MS})$ is $\sim 4.9\sigma$ and $\sim 4.6\sigma$, respectively. Our sample above redshift $z > 1.3$ is small, limited to 21 cluster and 42 field galaxies. We find no significant difference between the cluster and field $\log(\Delta SFR_{MS})$ and $\log(\Delta sSFR_{MS})$ for this small subsample.

---

[4]If we downsample the field to match that of the cluster galaxy sample size, we find similar values of significance (for 10 000 random subsamples, the median and mean significance is 2.8σ).

[5]In these redshift subset comparisons, we apply an SFR limit derived by converting the 80 per cent F([O II]) limit to an SFR at the higher redshift limit of the sample – i.e. $z = 1.3$ for the $1.0 < z < 1.3$ sample and $z = 1.5$ for the $1.3 < z < 1.5$ sample.

4 DISCUSSION

4.1 Environmental dependence of the star-forming MS

In this study, we identify an environmental dependence on the star-forming galaxy MS at $1.0 < z < 1.5$, where cluster galaxies have lower $\log \Delta SFR_{MS}$ at fixed stellar mass than their counterparts in the field by a factor of 1.4, with a significance in $\log \Delta SFR_{MS}$ of $\sim 3.3\sigma$ across all stellar masses, but strongest at lower stellar masses (Fig. 5).

Our findings are in good agreement with those of Noirot et al. (2018), who find a significant suppression in the MS of the CARLA cluster sample, relative to the field sample of Whitaker et al. (2014) at $z \sim 1.5$. However, our results appear to differ somewhat from some other studies at a comparable redshift. For example, Zeimann et al. (2013) use *HST* grism data to measure H α fluxes of galaxies in 18 clusters at $1.0 < z < 1.5$ and find no significant environmental dependence of the star-forming MS.

Comparing their H α-derived SF properties directly in a consistent manner with that of this paper, we find that the GOGREEN [O II]-derived ΔSFR_{MS} distributions are very similar to that of the H α-derived ΔSFR_{MS} from Zeimann et al. (2013). From a direct comparison of cluster and field ΔSFR_{MS} distributions, we see a hint that the cluster ΔSFR_{MS} are lower than the field at lower stellar masses, but in agreement with Zeimann et al. (2013), this difference is not statistically significant. We refer the reader to Appendix B for more details. Although the authors do observe that the H α equivalent widths (EWs) of the cluster star-forming galaxies are lower than their counterparts in the field for $M_* < 10^{10}$ M$_\odot$, they attribute this to a difference in SFH. They also find weak evidence that the dust content of cluster galaxies is lower than that in the field.

Using a sample of galaxy groups at $0.5 < z < 1.1$ from COSMOS, AEGIS, ECDFS, and CDFN fields, Erfanianfar et al. (2016) find little variation in the star-forming MS with environment. Our result also differs from other studies at a range of redshifts (e.g. Elbaz et al. 2007; Cooper et al. 2008; Popesso et al. 2011) which claim to observe a *reversal* of the sSFR-density trend, such that star-forming galaxies in dense environments have *higher* sSFR than the field. However, it is noted in these studies that the samples are dominated by groups rather than clusters, and so this reversal in the trend of sSFR density does not necessarily apply to massive clusters. Many of these results are also driven by higher mass galaxies, where dust corrections are most important. We note that Popesso et al. (2011) find a trend that is similar to the one we observe, when restricted to lower stellar mass galaxies.

Taken by itself, the environmental dependence on the star-forming galaxy MS that we find allows for numerous interpretations. In this work, we consider two possible interpretations: a formation time dependence on cluster and field populations, motivated by the results of van der Burg et al. (in preparation) and Webb et al. (in preparation); and a delayed-than-rapid quenching model based on Wetzel et al. (2013) that has shown to provide a good match to certain studies at lower redshift. While these scenarios are not necessarily the only interpretations possible given our observational results, they serve as useful reference points.

4.2 Formation time predictions

A simple scenario to explain the observed suppression in the cluster star-forming galaxy MS compared to that of the field without the need to invoke environmentally driven quenching in cluster
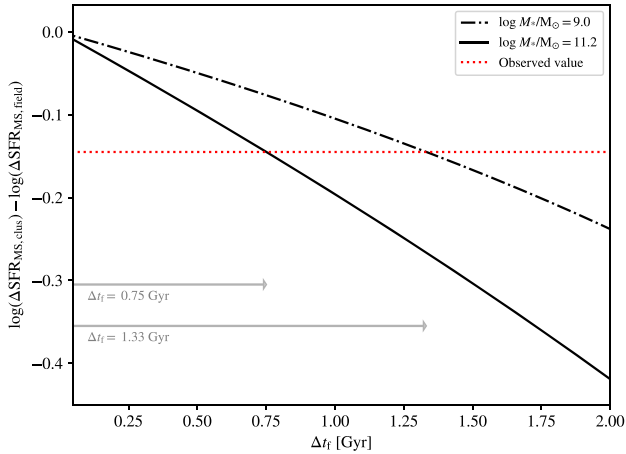
Figure 7. The average difference in formation time between cluster and field galaxies versus the difference in $\log(\Delta SFR_{MS})$ between the two samples. These values are derived from the Schreiber et al. (2015) cosmic SFR versus redshift relation, assuming two fiducial stellar masses located at the minimum (dashed dotted) and maximum (solid) ends of the stellar mass distribution of our sample. The red dotted line shows the observed $\log(\Delta SFR_{MS})$ difference between cluster and field.

environments is that cluster galaxies have simply formed earlier than field galaxies.[6]

To explore this scenario, we employ the Schreiber et al. (2015) cosmic SFR versus redshift relation to find the difference in redshift (and hence time) required to produce the observed difference between cluster and field $\log(\Delta SFR_{MS})$ of -0.145 $M_\odot$ yr^{-1}. In Fig. 7, we show an example of the formation time difference between cluster and field galaxies versus the resulting difference in $\log(\Delta SFR_{MS})$ for two fiducial stellar masses that are taken as the minimum (dashed dotted) and maximum (solid) stellar masses of galaxies in our sample. The red dotted line shows the observed $\log(\Delta SFR_{MS})$ difference between cluster and field, which corresponds to formation time differences of >0.75 Gyr for high-mass galaxies ($\log(M_*/M_\odot) \sim 11.2$) and >1.3 Gyr for low-mass galaxies ($\log(M_*/M_\odot) \sim 9.0$). While these formation time differences are long, requiring a substantial 'head start' for cluster galaxies compared to galaxies in the field, they are not inconsistent with works focussing on other observables such as the Fundamental Plane, for example, Saglia et al. (2010), who find differences in ages of cluster and field galaxies of ~ 1 Gyr at a fixed stellar mass and redshift using the EDisCS cluster sample. However, we note that other works also based on Fundamental Plane such as van Dokkum & van der Marel (2007) find smaller differences in the ages of stars in massive cluster galaxies compared to the field of ~ 0.4 Gyr.

4.3 Environmental quenching time-scale predictions

We now move to exploring an alternative scenario where a simple interpretation of our observations is that recently accreted cluster

[6]This scenario is not necessarily supported by assembly bias, where the relation between age and clustering depends on the halo mass relative to the characteristic collapse mass, M_c, at a given redshift. At $M_{vir} >> M_c$, younger haloes are clustered more strongly than older haloes, with the reverse being true at $M_{vir} << M_c$ (Wechsler et al. 2006; Gao & White 2007; Zentner, Hearin & van den Bosch 2014).

galaxies are undergoing an environmentally driven decline in star formation without the need to invoke a formation time difference between cluster and field galaxies. To try and quantify what the implied quenching rates would be, we consider a toy model based on Wetzel et al. (2013). In this model, after a satellite galaxy infalls into a cluster halo, there is a period of time referred to as the 'delay-time', t_{delay}, within which a galaxy's SFR follows that of the typical field evolution. After the delay-time, there is then a period of rapid decrease in SFR that declines at a rate defined by τ, often referred to as the 'fading time':

$$SFR = \begin{cases} SFR(t_{start})e^{(-(t-t_{start})/\tau)}, & t > t_{start} \\ SFR(t), & t \leq t_{start} \end{cases} \quad (8)$$

where $t_{start} = t_{infall} + t_{delay}$.

This 'delayed-then-rapid' quenching scenario is also supported by studies such as McCarthy et al. (2008) who find that satellite galaxies in hydro-dynamical simulations typically maintain a significant fraction of their hot gas after infall into the cluster potential. Mok et al. (2014), who study the Group Environment Evolution Collaboration 2 (GEEC2) sample of galaxy groups at $0.8 < z < 1.0$, also find that it is necessary to invoke a model that includes a period of typical field SF activity before rapidly quenching to explain the observed fractions of star-forming/intermediate/quiescent fractions (a no delay scenario would require longer fading times that would overproduce intermediate-colour galaxies).
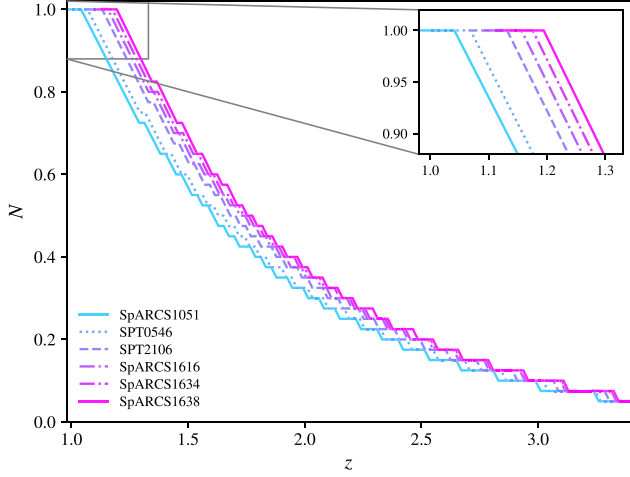
It is our goal to constrain the parameters t_{delay} and τ in this model using the measured properties of cluster and field galaxies. We choose to focus on galaxies in both the observed cluster and field population with $\log M_*/M_\odot < 10.3$ and at $1.0 < z < 1.3$ in an effort to restrict our study to satellite galaxies where we expect quenching is not dominated by internal processes (unlike massive galaxies), and where our [O II]-derived SFRs are expected to be most robust given the lower dust extinction.

We first generate a parent sample of galaxies whose infall redshifts correspond to the time at which the galaxies were accreted into the cluster. We employ a physically motivated distribution of infall redshifts, following Neistein, van den Bosch & Dekel (2006) and Neistein & Dekel (2008), and use a functional form of the average mass accretion history similar to that of the main progenitor (MP) halo in the Extended Press-Schechter formalism (Press & Schechter 1974; Bond et al. 1991; Lacey & Cole 1993).[7] For more details regarding how this infall redshift distribution was generated, we refer the reader to Appendix C. We show the cumulative distribution of accretion redshifts for the modelled galaxies for each of the six clusters at $z < 1.3$ in Fig. 8.

We use the observed field sample, with 50 random selections per cluster member and evolve their SFRs to these infall redshifts, via the Schreiber et al. (2015) relation described in Section 2.6. To be able to compare this model cluster population to the observed cluster distribution, we then evolve their SFRs from the assigned infall redshifts forwards to the parent cluster redshift according to a range of t_{delay} and τ time-scales. Our aim is to exclude unlikely combinations of t_{delay} and τ by deducing which resulting SFR

[7]In this model, mass accretion history is based on when a galaxy is accreted into the most massive halo; that is, this model does not consider the effect of group pre-processing. Alternatively, if massive accretion is based on when galaxy first becomes a satellite, we would expect longer delay time-scales.

Figure 8. Cumulative distributions of physically motivated accretion redshifts for the modelled galaxies based on six clusters at $z < 1.3$, described in further in detail in Section 4.3. The location where the curves plateau corresponds to the observed cluster redshift.

Figure 9. In this figure, we present density contours showing the likely range of quenching time-scale parameters t_{delay} and τ, adopted in the toy model derived from the observed difference between the GOGREEN cluster galaxy and field star-forming galaxy MS. The density contours are derived from the two-sample KS-test p-values comparing the observed GOGREEN cluster galaxy SFR distribution and the predicted field distribution. Note that these distributions have been subtracted from the main-sequence relation for cluster and field galaxies. Lower two-sample KS test p-values indicate more absolute maximum distance between the cumulative distribution functions of the two samples, and therefore more less time-scale values. The left subplot shows the quenching time-scales based on Model 1 from equation (8), and the right subplot shows quenching timescales based off of Model 2 from equation (9). The opaque region in the lower corner below the dashed grey line signifies the time-scale parameter space where the fraction of model star-forming galaxies that drop below the $F([O\,\textsc{ii}])$ limit ($F([O\,\textsc{ii}]) = 2.2 \times 10^{-17}\,\mathrm{erg\,cm^{-2}\,s^{-1}}$), $f_{dropout}$, is >0.8, and the opaque region in the upper corner above the dotted grey line signifies the time-scale parameter space where $f_{dropout}$ is <0.1.

distributions are significantly different from the observed cluster galaxy SFR distribution.[8]

We use the MS fit described in Section 3 to calculate a $\Delta\mathrm{SFR_{clus}}$ distribution for both the observed cluster galaxies and the model cluster population, $\Delta\mathrm{SFR_{model\,clus}}$, for all time-scales. For each time-scale realization, we then perform a two-sample KS test on the observed cluster galaxy distribution and the model cluster population distribution i.e. KS($\Delta\mathrm{SFR_{clus}}$, $\Delta\mathrm{SFR_{model\,clus}}$) to test against the null hypothesis that two independent samples are drawn from the same continuous distribution. Higher two-sample KS test p-values indicate a smaller absolute maximum distance between the cumulative distribution functions of the two samples, and therefore more likely time-scale values.

In addition to the parametrization of the delayed-then-rapid quenching model described in equation (8), we also present an alternative parametrization following from Hahn, Tinker & Wetzel (2017)[9], where
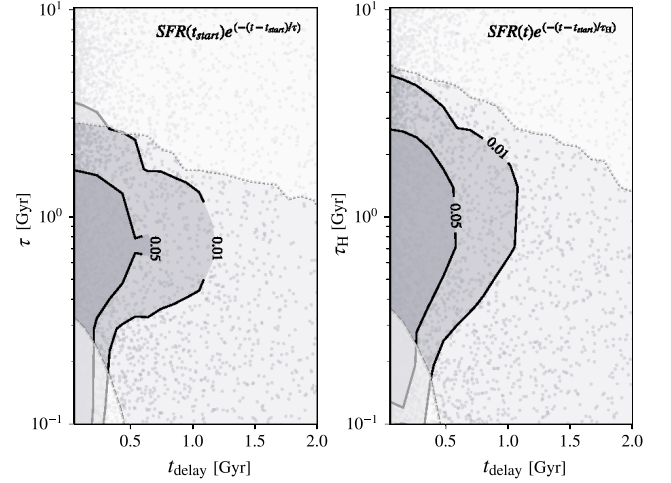
$$\mathrm{SFR} = \begin{cases} \mathrm{SFR}(t)e^{(-(t-t_{start})/\tau_H)}, & t > t_{start} \\ \mathrm{SFR}(t), & t \leq t_{start}. \end{cases} \quad (9)$$

In the first parametrization, equation (8), τ represents the SFR evolution during the quenching epoch ($t > (t_{infall} + t_{delay})$). In the absence of environmental effects, $\tau < \infty$ as the SFRs of the field galaxies evolve.[10] In the second parametrization, equation (9), τ_H represents the additional quenching on top of the normal SFR evolution, and is therefore a clearer indicator of the role of environmental quenching. We opt to present results of both models to allow us to compare with different environmental quenching time-scales presented in the literature.

In Fig. 9, we show the resulting quenching time-scale parameter space density contours for 10 000 simulations of different t_{delay} and τ produced with the two parametrizations. Examples of resulting < $\Delta\log\mathrm{SFR_{MS}}$ > distributions for specific t_{delay} and τ time-scales can be found in Fig. A1 in the Appendix. The opaque region in the lower corner below the dashed grey line signifies the time-scale parameter space where the fraction of model star-forming galaxies that drop below the $F([O\,\textsc{ii}])$ limit ($F([O\,\textsc{ii}]) = 2.2 \times 10^{-17}\,\mathrm{erg\,cm^{-2}\,s^{-1}}$), $f_{dropout}$, is >0.8, and the opaque region in the upper corner above the dotted grey line signifies the time-scale parameter space where $f_{dropout}$ is <0.1. Given that quenched fraction excesses are unlikely to be as high as 0.8 or as low as 0.1 (van der Burg et al. in preparation), we see that a combination of a short delay and short fade time is unlikely given this conservative dropout fraction. If, in reality, the quenched fraction is lower than that assumed here, we would expect a further restriction in this region in quenching time-scale parameter space.

We constrain $t_{delay} < 1.2$ Gyr at the 99 per cent level. For very rapid quenching scenarios, the constraint on the delay time is stronger ($t_{delay} < 0.25$ Gyr at the 99 per cent level). We find that the time-scale for environmental quenching is $\tau_H < 6$ Gyr, allowing for modest environmental quenching, as long as delay times are reasonably short, so that a significant population of galaxies are affected. At face value, given the broad constraints shown in Fig. 9 on t_{delay}, we cannot rule out a slow-quenching scenario where

---

[8]Note that by construction, if there is no environmental quenching, the model cluster SFR distribution should end up looking exactly like the observed field.

[9]In Hahn et al. (2017), this parametrization is adopted for central galaxies, while here we use this parametrization for satellite galaxies.

[10]Analytically, in the absence of environmental effects, τ exists only if $t > t_{start}$, but when fitting the model to data, there is a degeneracy between a long t_{delay} and a τ equal to the effective SFR decline of the field population.

galaxies quench slowly from infall at a rate that is accelerated somewhat in comparison to the field. The time-scales we constrain are in general agreement with works such as Muzzin et al. (2014) and Mok et al. (2014), who derive constraints using galaxy cluster phase space and fractions of red, blue, and green galaxies, respectively, in samples of clusters at $0.8 < z < 1.0$. However, there is a hint that our short delay time-scale predictions could be in tension with some works that favour longer delay times. For example, Balogh et al. (2016) find delay times of ~4.5 Gyr at $z = 0$ for galaxies in a similar mass range (assuming fixed fading time of ~0.5 Gyr), which would correspond to ~1.3 Gyr if the delay time-scales with the dynamical time.

We note again that different time-scale combinations would lead to very different quenched fractions. For example, short delay times combined with short fade times would result in almost all cluster galaxies being quenched, while very long delay times combined with long tau would lead to implausibly small quenched fractions. Combining the constraints from this work with our analysis of the stellar mass functions (Reeves et al. in preparation; van der Burg et al. in preparation) will lead to much tighter constraints on these time-scales.

An important caveat of this delay time-scale modelling is that we assume that dust content of cluster and field galaxies are the same, and that the difference we observe between cluster and field galaxies is due to a difference in SFH. Zeimann et al. (2013) find that at fixed stellar mass, field star-forming galaxies have slightly higher extinction on average than star-forming galaxies in clusters (though the difference is within their error bars). If dust extinction is higher for field galaxies compared to cluster galaxies in this study, the difference in the star-forming galaxy MS would be underestimated, and we would expect shorter delay times and/or longer fading times than those predicted by this toy model.

We also note it is likely that our cluster sample contains a certain number of interloping galaxies that are not gravitationally bound to the cluster but are mistaken for cluster members. Even for large, well-sampled cluster galaxy spectroscopic samples, the interloper rate for dynamical membership techniques is predicted to be at least 15 per cent (Duarte & Mamon 2015; Wojtak et al. 2018). The impact of interloping galaxies is expected to dilute any environmental dependence of the star-forming galaxy MS, which would also result in a larger difference in the MS between cluster and field and therefore require shorter delay times and/or longer fading times than those predicted by this toy model.

5 CONCLUSIONS

In this paper, we explore the environmental dependence of the star-forming galaxy MS in an unprecedented sample of homogeneously selected deep spectroscopic observations of galaxies in 11 galaxy cluster fields at $1.0 < z < 1.5$ from the GOGREEN survey. Our major findings can be summarized as follows:

(i) We take a Bayesian model approach in detecting [O II] emission from the GOGREEN galaxy spectra, employing BIC to distinguish cases where there is strong evidence supporting a model with [O II] emission over a model with no emission, taking into account the noise properties of the continuum in each individual spectrum. Employing a conservative F([O II]) limit, we detect [O II] emission in 100 cluster galaxies and 162 field galaxies across 11 of the GOGREEN cluster fields.

(ii) When accounting for differences between cluster and field redshift properties, we find that the cluster galaxy MS is lower compared to that of the field galaxy MS at $1.0 < z < 1.5$, with a difference of ~3.3σ. We find that this result is driven by the lower redshift end of the sample, and is more significant for lower stellar mass galaxies.

(iii) This observed environmental dependence on the star-forming galaxy MS allows for numerous interpretations. We explore several of these scenarios, placing constraints based on our measurements. One such interpretation is that cluster galaxies are simply formed earlier than field galaxies. Given our observations, long formation time differences between the two populations of >0.8 Gyr would be required in this interpretation. Focussing on an alternative scenario whereby environmentally induced quenching occurs, we model the likely quenching time-scales given the size of the observed difference between the cluster and field MS, and find that our data favour delay times of <1.2 Gyr at the 99 per cent level.

The formation time and star formation quenching time-scale constraints from this work will be combined with analysis of the stellar mass functions of galaxy clusters (van der Burg et al. in preparation), galaxy groups (Reeves et al. in preparation) and quiescent galaxy stellar population ages (Webb et al. in preparation) from the GOGREEN survey, providing tighter constraints on models of galaxy evolution in dense environments.

(Foreman-Mackey et al. 2013), MATPLOTLIB (Hunter 2007), and NUMPY (Oliphant 2015).

REFERENCES

Abazajian K. N. et al., 2009, ApJS, 182, 543
Ashman K. M., Bird C. M., Zepf S. E., 1994, AJ, 108, 2348
Astropy Collaboration et al., 2013, A&A, 558, A33
Astropy Collaboration et al., 2018, AJ, 156, 123
Baldry I. K., Glazebrook K., Brinkmann J., Ivezić Ž., Lupton R. H., Nichol R. C., Szalay A. S., 2004, ApJ, 600, 681
Balogh M. et al., 2004a, MNRAS, 348, 1355
Balogh M. L., Baldry I. K., Nichol R., Miller C., Bower R., Glazebrook K., 2004b, ApJ, 615, L101
Balogh M. L. et al., 2016, MNRAS, 456, 4364
Balogh M. L. et al., 2017, MNRAS, 470, 4168
Beers T. C., Gebhardt K., Forman W., Huchra J. P., Jones C., 1991, AJ, 102, 1581
Bond J. R., Cole S., Efstathiou G., Kaiser N., 1991, ApJ, 379, 440
Brodwin M. et al., 2010, ApJ, 721, 90
Bruzual G., Charlot S., 2003, MNRAS, 344, 1000
Calzetti D., Armus L., Bohlin R. C., Kinney A. L., Koornneef J., Storchi-Bergmann T., 2000, ApJ, 533, 682
Cassata P. et al., 2008, A&A, 483, L39
Chabrier G., 2003, PASP, 115, 763
Chartab N. et al., 2020, ApJ, 890, 7
Cimatti A. et al., 2008, A&A, 482, 21
Cooper M. C. et al., 2006, MNRAS, 370, 198
Cooper M. C. et al., 2007, MNRAS, 376, 1445
Cooper M. C. et al., 2008, MNRAS, 383, 1058
Davies L. J. M. et al., 2016, MNRAS, 455, 4013
Demarco R. et al., 2010, ApJ, 711, 1185
Duarte M., Mamon G. A., 2015, MNRAS, 453, 3848
Elbaz D. et al., 2007, A&A, 468, 33
Erfanianfar G. et al., 2016, MNRAS, 455, 2839
Fadda D., Girardi M., Giuricin G., Mardirossian F., Mezzetti M., 1996, ApJ, 473, 670
Fillingham S. P., Cooper M. C., Wheeler C., Garrison-Kimmel S., Boylan-Kolchin M., Bullock J. S., 2015, MNRAS, 454, 2039
Finoguenov A. et al., 2007, ApJS, 172, 182
Finoguenov A. et al., 2010, MNRAS, 403, 2063
Foley R. J. et al., 2011, ApJ, 731, 86
Foltz R. et al., 2018, ApJ, 866, 136
Foreman-Mackey D., Hogg D. W., Lang D., Goodman J., 2013, PASP, 125, 306
Fossati M. et al., 2017, ApJ, 835, 153
Galametz A. et al., 2013, ApJS, 206, 10
Gallazzi A. et al., 2009, ApJ, 690, 1883
Gao L., White S. D. M., 2007, MNRAS, 377, L5
Gao L., Navarro J. F., Cole S., Frenk C. S., White S. D. M., Springel V., Jenkins A., Neto A. F., 2008, MNRAS, 387, 536
George M. R. et al., 2011, ApJ, 742, 125
Gilbank D. G., Baldry I. K., Balogh M. L., Glazebrook K., Bower R. G., 2010, MNRAS, 405, 2594
Gimeno G. et al., 2016, Proc. SPIE, 9908, 99082S
Girardi M., Biviano A., Giuricin G., Mardirossian F., Mezzetti M., 1993, ApJ, 404, 38
Gobat R., Rosati P., Strazzullo V., Rettura A., Demarco R., Nonino M., 2008, A&A, 488, 853
Guglielmo V. et al., 2019, A&A, 625, A112
Hahn C., Tinker J. L., Wetzel A., 2017, ApJ, 841, 6
Haines C. P. et al., 2013, ApJ, 775, 126
Hayashi M., Sobral D., Best P. N., Smail I., Kodama T., 2013, MNRAS, 430, 1042
Hinton S. R., Davis T. M., Lidman C., Glazebrook K., Lewis G. F., 2016, Astron. Comput., 15, 61

Hook I. M., Jørgensen I., Allington-Smith J. R., Davies R. L., Metcalfe N., Murowinski R. G., Crampton D., 2004, PASP, 116, 425
Hunter J. D., 2007, CSE, 9, 90
Kass R. E., Raftery A. E., 1995, J. Am. Stat. Assoc., 90, 773
Kauffmann G. et al., 2003, MNRAS, 346, 1055
Kauffmann G., White S. D. M., Heckman T. M., Ménard B., Brinchmann J., Charlot S., Tremonti C., Brinkmann J., 2004, MNRAS, 353, 713
Kausch W. et al., 2015, A&A, 576, A78
Kawinwanichakij L. et al., 2017, ApJ, 847, 134
Kimm T. et al., 2009, MNRAS, 394, 1131
Koyama Y. et al., 2013, MNRAS, 434, 423
Kriek M., van Dokkum P. G., Labbé I., Franx M., Illingworth G. D., Marchesini D., Quadri R. F., 2009, ApJ, 700, 221
Kriek M. et al., 2018, Astrophysics Source Code Library, record ascl:1803.008
Lacey C., Cole S., 1993, MNRAS, 262, 627
Leja J., Carnall A. C., Johnson B. D., Conroy C., Speagle J. S., 2019a, ApJ, 876, 3
Leja J. et al., 2019b, ApJ, 877, 140
Lotz J. M. et al., 2013, ApJ, 773, 154
Macciò A. V., Dutton A. A., van den Bosch F. C., 2008, MNRAS, 391, 1940
Madau P., Dickinson M., 2014, ARA&A, 52, 415
Mamon G. A., Boué G., 2010, MNRAS, 401, 2433
Mamon G. A., Biviano A., Boué G., 2013, MNRAS, 429, 3079
Martini P. et al., 2013, ApJ, 768, 1
Matharu J. et al., 2019, MNRAS, 484, 595
Mauduit J. C. et al., 2012, PASP, 124, 714
McCarthy I. G., Frenk C. S., Font A. S., Lacey C. G., Bower R. G., Mitchell N. L., Balogh M. L., Theuns T., 2008, MNRAS, 383, 593
McGee S. L., Balogh M. L., 2010, MNRAS, 405, 2069
McGee S. L., Bower R. G., Balogh M. L., 2014, MNRAS, 442, L105
McLachlan G. J., Basford K. E., 1988, Mixture Models. Inference and Applications to Clustering. Marcel Dekker, New York
Mok A. et al., 2013, MNRAS, 431, 1090
Mok A. et al., 2014, MNRAS, 438, 3070
Murowinski R. G. et al., 1998, Proc. SPIE, 3355, 188
Muzzin A. et al., 2009, ApJ, 698, 1934
Muzzin A. et al., 2012, ApJ, 746, 188
Muzzin A. et al., 2013, ApJS, 206, 8
Muzzin A. et al., 2014, ApJ, 796, 65
Nanayakkara T. et al., 2016, ApJ, 828, 21
Nantais J. B., Rettura A., Lidman C., Demarco R., Gobat R., Rosati P., Jee M. J., 2013, A&A, 556, A112
Nantais J. B. et al., 2017, MNRAS, 465, L104
Navarro J. F., Frenk C. S., White S. D. M., 1997, ApJ, 490, 493
Neistein E., Dekel A., 2008, MNRAS, 383, 615
Neistein E., van den Bosch F. C., Dekel A., 2006, MNRAS, 372, 933
Newman A. B., Ellis R. S., Andreon S., Treu T., Raichoor A., Trinchieri G., 2014, ApJ, 788, 51
Noeske K. G. et al., 2007, ApJ, 660, L43
Noirot G. et al., 2018, ApJ, 859, 38
Oliphant T. E., 2015, Guide to NumPy, 2nd edn. Create Space Independent Publishing Platform, USA
Oman K. A., Hudson M. J., 2016, MNRAS, 463, 3083
Paccagnella A. et al., 2016, ApJ, 816, L25
Patel S. G., Kelson D. D., Holden B. P., Franx M., Illingworth G. D., 2011, ApJ, 735, 53
Peng Y.-j. et al., 2010, ApJ, 721, 193
Pintos-Castro I., Yee H. K. C., Muzzin A., Old L., Wilson G., 2019, ApJ, 876, 40
Poggianti B. M. et al., 2006, ApJ, 642, 188
Popesso P. et al., 2011, A&A, 532, A145
Press W. H., Schechter P., 1974, ApJ, 187, 425
Rodríguez del Pino B. et al., 2017, MNRAS, 467, 4200
Saglia R. P. et al., 2010, A&A, 524, A6
Sanders D. B. et al., 2007, ApJS, 172, 86
Schreiber C. et al., 2015, A&A, 575, A74

Schwarz G., 1978, Annals Statist., 6, 461

Sen P. K., 1968, J. Am. Stat. Assoc., 63, 1379

Smette A. et al., 2015, A&A, 576, A77

Snyder G. F. et al., 2012, ApJ, 756, 114

Sobral D., Best P. N., Matsuda Y., Smail I., Geach J. E., Cirasuolo M., 2012, MNRAS, 420, 1926

Stalder B. et al., 2013, ApJ, 763, 93

Stanford S. A., Gonzalez A. H., Brodwin M., Gettings D. P., Eisenhardt P. R. M., Stern D., Wylezalek D., 2014, ApJ, 213, 25

Strateva I. et al., 2001, AJ, 122, 1861

Strazzullo V. et al., 2006, A&A, 450, 909

Strazzullo V. et al., 2019, A&A, 622, A117

Tacconi L. J. et al., 2013, ApJ, 768, 74

Tacconi L. J. et al., 2018, ApJ, 853, 179

Taranu D. S., Hudson M. J., Balogh M. L., Smith R. J., Power C., Oman K. A., Krane B., 2014, MNRAS, 440, 1934

Taylor E. N. et al., 2015, MNRAS, 446, 2144

Theil H., 1950, Proceedings of Koninklijke Nederlandse Akademie Wetenschappen, Series A Mathematical Sciences. p. 386

Tinker J. L., Wetzel A. R., 2010, ApJ, 719, 88

Tinker J. L., Leauthaud A., Bundy K., George M. R., Behroozi P., Massey R., Rhodes J., Wechsler R. H., 2013, ApJ, 778, 93

van Dokkum P. G., van der Marel R. P., 2007, ApJ, 655, 30

Virtanen P. et al., 2019, preprint (arXiv:1907.10121)

von der Linden A., Wild V., Kauffmann G., White S. D. M., Weinmann S., 2010, MNRAS, 404, 1231

Vulcani B., Poggianti B. M., Finn R. A., Rudnick G., Desai V., Bamford S., 2010, ApJ, 710, L1

Wang L. et al., 2018, A&A, 618, A1

Wechsler R. H., Zentner A. R., Bullock J. S., Kravtsov A. V., Allgood B., 2006, ApJ, 652, 71

Wetzel A. R., Tinker J. L., Conroy C., 2012, MNRAS, 424, 232

Wetzel A. R., Tinker J. L., Conroy C., van den Bosch F. C., 2013, MNRAS, 432, 336

Whitaker K. E., van Dokkum P. G., Brammer G., Franx M., 2012, ApJ, 754, L29

Whitaker K. E. et al., 2014, ApJ, 795, 104

Wijesinghe D. B. et al., 2012, MNRAS, 423, 3679

Williams R. J., Quadri R. F., Franx M., van Dokkum P., Labbé I., 2009, ApJ, 691, 1879

Wilson G. et al., 2009, ApJ, 698, 1943

Wojtak R. et al., 2018, MNRAS, 481, 324

Yang X., Mo H. J., van den Bosch F. C., Jing Y. P., 2005, MNRAS, 356, 1293

York D. G. et al., 2000, AJ, 120, 1579

Zeimann G. R. et al., 2013, ApJ, 779, 137

Zentner A. R., Hearin A. P., van den Bosch F. C., 2014, MNRAS, 443, 3044

APPENDIX A: CLUSTER MEMBERSHIP ALGORITHMS

In this section, we describe the two algorithms used to define cluster membership. First, the main cluster redshift peak is identified by selecting those galaxies in the cluster field with $c|z - z_c| \leq 6000\,\mathrm{km\,s^{-1}}$ (as in Beers et al. 1991; Girardi et al. 1993). Here, c is the speed of light and z_c is the cluster redshift estimate from Balogh et al. (2017). To try to identify cases of merging subclusters close to the line of sight, and when these cases occur, to separate these subcluster components from the main cluster, the KMM algorithm is applied to the distribution of redshifts located in the main peak. The algorithm estimates the probability that the z distribution is better represented by k Gaussians rather than a single Gaussian (McLachlan & Basford 1988; Ashman, Bird & Zepf 1994).

With the resulting galaxies left after the main-peak and KMM selection procedures, cluster membership is then refined using two techniques, Clean (Mamon et al. 2013) and C.L.U.M.P.S (Munari et al. in preparation). Both these algorithms identify cluster members based on their location in projected phase space, Rv_{rf}, where R is the projected radial distance from the cluster centre, and $v_{\mathrm{rf}} \equiv c(z - \bar{z})/(1 + \bar{z})$ is the rest-frame velocity. While these two algorithms are both based in projected phase space, they are conceptually very different.

The Clean algorithm is theoretically motivated, with its parameters fixed by properties of cluster-sized haloes extracted from cosmological numerical simulations. The Clean method uses an estimate of the cluster line-of-sight velocity dispersion σ_{los}, to predict the cluster mass from a scaling relation. The algorithm then adopts a NFW profile (Navarro, Frenk & White 1997), a theoretical concentration-mass relation (Macciò, Dutton & van den Bosch 2008), and a velocity anisotropy profile model (Mamon & Boué 2010), to predict $\sigma_{\mathrm{los}}(R)$, and to iteratively reject galaxies with $|v_{\mathrm{rf}}| > 2.7\sigma_{\mathrm{los}}$ at any radius.

The C.L.U.M.P.S algorithm is based only on the fact that clusters of galaxies manifest themselves as concentrations in project phase space, and so by nature, it is less model-dependent than the Clean algorithm. The C.L.U.M.P.S is based on the Shifting Gapper (SG) method of Fadda et al. (1996), however, is more robust to the SG method with respect to the choice of the initial parameters that define the smoothing lengths in projected phase space. The C.L.U.M.P.S method evaluates the density of galaxies in projected phase space
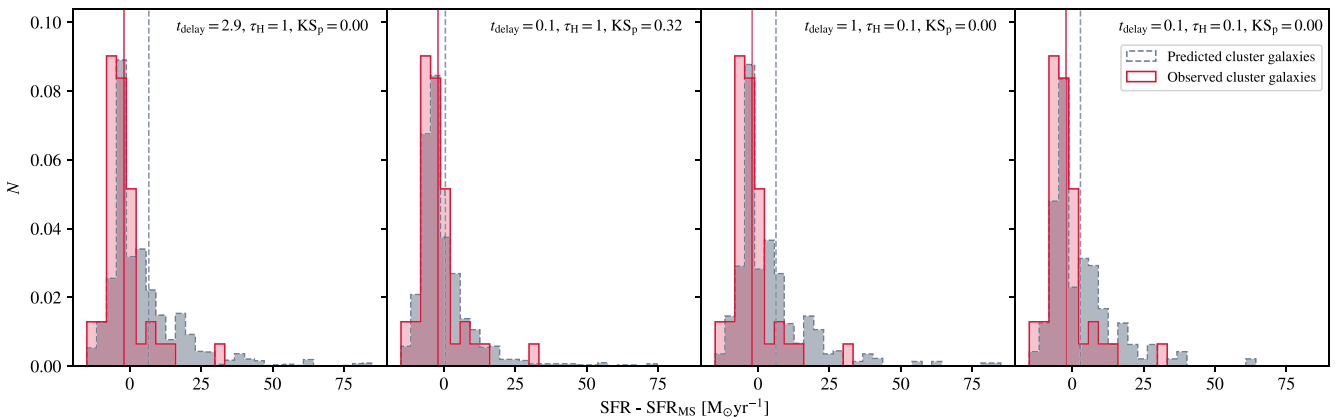
Figure A1. Example toy model-predicted cluster and observed cluster ΔSFR_{MS} distributions for different τ_H and t_{delay} timescales.

and convolves this density map with a Gaussian filter in Fourier space to remove high frequencies. The technique then bins this smoothed density along the radial direction to identify the main peak in velocity space. The minima of this peak define the velocity limits within which to include cluster members in that given radial bin. We note that the method is still being refined and tested (Munari et al. in preparation).
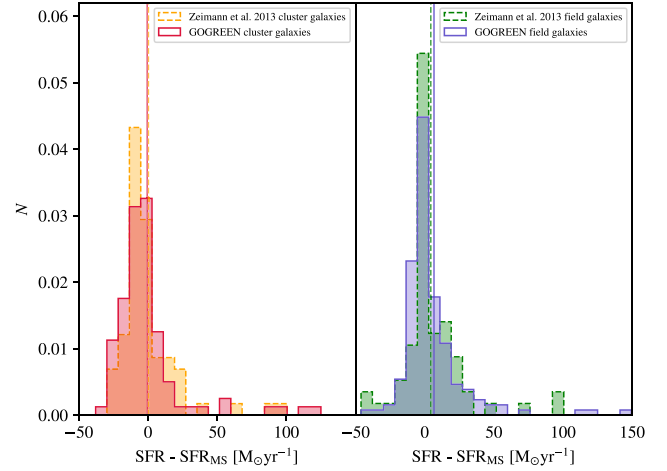
These two algorithms are applied to the data twice, the first time where $\bar{z}$ is defined as the average redshift of the galaxies that were selected during the main-peak and KMM procedures, and the second time where $\bar{z}$ is defined as the average redshift of the galaxies selected as members from the first run. The radius, r_{200c}, is obtained from σ_{los} and equation B3 in Mamon et al. (2013) in an iterative procedure, where we assume the Mamon & Boué (2010) velocity anisotropy profile, and a NFW profile model for the mass distribution with a concentration taken to be $c_{200} = 5$ on the first iteration, and derived from the concentration–mass relation of Gao et al. (2008) on subsequent iterations. In this paper, cluster members are defined as those that are identified by either the Clean or C.L.U.M.P.S algorithm.

The number of galaxies identified by the Clean algorithm as cluster and field are 84 and 164, respectively, whilst the number of galaxies identified by the C.L.U.M.P.S algorithm are 79 and 184. We find no significant difference in the stellar mass and cluster-centric radial distributions of both the field and cluster galaxy samples selected by either of these membership algorithms.[11] We also confirm that all of the conclusions in this work remain regardless of whether the membership is defined using both the Clean and C.L.U.M.P.S algorithms or solely the Clean or C.L.U.M.P.S algorithm.

APPENDIX B: COMPARISON TO H α-DERIVED SFRS

To further explore our findings regarding the environmental dependence of the star-forming MS in the context of studies at the same epoch derived from SFR proxies other then [O II] emission, we compare with data from Zeimann et al. (2013). In this study, Zeimann et al. (2013) compare the star-forming MS of galaxies across 18 galaxy clusters at $1.0 < z < 1.5$. We perform the same procedure as described in Section 3, using the full galaxy GOGREEN sample MS relation to calculate ΔSFR_{MS} values for 71 cluster and 71 field galaxies from Zeimann et al. (2013).

From Fig. B1, we see that the [O II]-derived GOGREEN and H α-derived Zeimann et al. (2013) ΔSFR_{MS} distributions (*right*) are remarkably similar in terms of the mean ΔSFR_{MS}. We also directly compare the [O II]-derived GOGREEN and H α-derived Zeimann et al. (2013) star-forming MS, again finding remarkable agreement between the [O II]-derived and H α-derived SFRs. As discussed in Zeimann et al. (2013), there is no significant difference between cluster and field star-forming MS in the Zeimann et al. (2013) sample.

<hr/>

[11]A two-sample KS test does not reject the null hypothesis that the cluster samples produced by the two membership algorithms are drawn from the same distribution with a p-values of >0.99 for both stellar mass and cluster-centric radius. The same is also found for the field samples produced by the membership algorithms.

Figure B1. [O II]-derived GOGREEN cluster (solid) ΔSFR_{MS} distribution and H α-derived Zeimann et al. (2013) cluster (dashed) ΔSFR_{MS} distribution (*left*). GOGREEN field (solid) and Zeimann et al. (2013) field (dashed) ΔSFR_{MS} distributions are shown on the *right*.
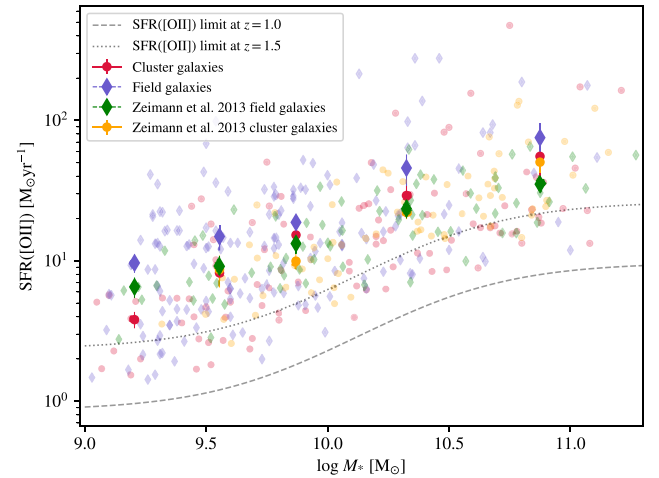
Figure B2. [O II]-derived MS of star formation of cluster galaxies versus field galaxies in the GOGREEN fields, along with the H α-derived MS from Zeimann et al. (2013). The solid purple and crimson markers signify the mean GOGREEN field SFRs and the GOGREEN cluster galaxy SFRs in each stellar mass bin, respectively. The solid orange and green markers signify the mean Zeimann et al. (2013) field SFRs and the Zeimann et al. (2013) cluster galaxy SFRs in each stellar mass bin, respectively. The GOGREEN field SFRs have been corrected using the cosmic SFR versus z relation of equation (7) in order to match the mean redshift of GOGREEN cluster galaxies within each stellar mass bin. The error bars represent the bootstrap standard error from bootstrap resampling the data within each bin. The dashed and dotted grey lines represent the SFRs that correspond to the 80 per cent flux completeness limit at $z = 1.0$ and $z = 1.5$, respectively.

APPENDIX C: TOY MODEL CLUSTER INFALL REDSHIFT DISTRIBUTION

In order to generate a parent sample of galaxies whose infall redshifts correspond to the time at which the galaxies were accreted into the cluster, we employ a physically motivated distribution of infall redshifts, following Neistein et al. (2006) and Neistein & Dekel (2008), using a functional form of the average mass accretion history similar to that of the main progenitor (MP) halo in the

Extended Press-Schechter formalism (Press & Schechter 1974; Bond et al. 1991; Lacey & Cole 1993), where the growth rate is given by

$$\frac{dM_{12}}{d\omega} = -\alpha M_{12}^{1+\beta}, \tag{C1}$$

where the time variable, $\omega \equiv \delta_c(z)/D(z)$ with $\delta_c(z) \simeq 1.69$ and $D(z)$ is the cosmological linear growth rate. In this parametrization, $M_{12} = \langle M_1 \rangle / 10^{12} h^{-1} \mathrm{M}_\odot$ where $\langle M_1 \rangle$ is the average mass of the MP. The best-fitting parameters derived from the halo statistics in the millennium simulation are $\alpha = 0.59$ and $\beta = 0.141$. The growth rate can be expressed in terms of time via

$$\frac{dM_{12}}{dt} = \dot{\omega} \frac{dM_1}{d\omega}, \tag{C2}$$

where $\dot{\omega}$ is approximated as

$$\dot{\omega} = -0.0470[1 + z + 0.1(1 + z)^{1.25}]^{2.5} h_{73} \, \mathrm{Gyr}^{-1}. \tag{C3}$$

We link the smooth accretion of mass growth over time to the accretion of galaxies by assigning infall redshifts to the model galaxy population in a manner that ensures that the slope of the redshift versus halo mass growth relation matches the slope of the infall redshift distribution of the model galaxy population.

[1]*European Space Agency (ESA), European Space Astronomy Centre, Villanueva de la Cañada, E-28691 Madrid, Spain*

[2]*Department of Astronomy & Astrophysics, University of Toronto, Ontario M5S 3H4, Toronto, Canada*

[3]*Department of Physics and Astronomy, University of Waterloo, Waterloo, Ontario N2L 3G1, Canada*

[4]*Waterloo Centre for Astrophysics, University of Waterloo, Waterloo, Ontario N2L3G1, Canada*

[5]*European Southern Observatory, Karl-Schwarzschild-Str. 2, D-85748, Garching, Germany*

[6]*INAF – Osservatorio Astronomico di Trieste, via G. B. Tiepolo 11, I-34143 Trieste, Italy*

[7]*IFPU – Institute for Fundamental Physics of the Universe, via Beirut 2, I-34014 Trieste, Italy*

[8]*Department of Physics and Astronomy, York University, 4700 Keele Street, Toronto, Ontario ON MJ3 1P3, Canada*

[9]*Department of Physics and Astronomy, The University of Kansas, 1251 Wescoe Hall Drive, Lawrence, KS 66045, USA*

[10]*INAF – Osservatorio astronomico di Padova, Vicolo Osservatorio 5, I-35122 Padova, Italy*

[11]*Department of Physics and Astronomy, University of California, Irvine, 4129 Frederick Reines Hall, Irvine, CA 92697, USA*

[12]*Steward Observatory and Department of Astronomy, University of Arizona, Tucson, AZ 85719, USA*

[13]*Departamento de Astronomía, Facultad de Ciencias Físicas y Matemáticas, Universidad de Concepción, Concepción, Chile*

[14]*Department of Physics and Astronomy, University of California, Riverside, 900 University Avenue, Riverside, CA 92521, USA*

[15]*Australian Astronomical Observatory, 105 Delhi Road, North Ryde, NSW 2113, Australia*

[16]*School of Physics and Astronomy, University of Birmingham, Edgbaston, Birmingham B15 2TT, England*

[17]*South African Astronomical Observatory, PO Box 9, Observatory 7935 Cape Town, South Africa*

[18]*Centre for Space Research, North-West University, Potchefstroom 2520 Cape Town, South Africa*

[19]*Astrophysics Research Institute, Liverpool John Moores University, 146 Brownlow Hill, Liverpool L3 5RF, UK*

[20]*Laboratoire d'astrophysique, École Polytechnique Fédérale de Lausanne, 1290 Versoix, Switzerland*

[21]*Departamento de Ciencias Físicas, Universidad Andres Bello, Fernandez Concha 700, Santiago, Región Metropolitana, Las Condes 7591538, Chile*

[22]*Arizona State University, School of Earth and Space Exploration, Tempe, AZ 871404, USA*

[23]*MIT Kavli Institute for Astrophysics and Space Research, 70 Vassar St, Cambridge, MA 02109, USA*

[24]*Department of Physics, McGill University, 3600 rue University, Montréal, Québec H3P 1T3, Canada*

This paper has been typeset from a TEX/LATEX file prepared by the author.